Catalysis Letters, Vol. 116, Nos. 3–4, August 2007 (© 2007)
DOI: 10.1007/s10562-007-9105-x

Phase transformation in CeO_2–Co_3O_4 binary oxide under reduction and calcination pretreatments

Chih-Wei Tang,[a,b] Wen-Yueh Yu,[b] Chin-Jung Lin,[b] Chen-Bin Wang,[a,*] and Shu-Hua Chien[b,c,*]

[a]*Department of Applied Chemistry and Materials Science, Chung Cheng Institute of Technology, National Defense University, Tahsi, Taoyuan, 33509 Taiwan, ROC*
[b]*Institute of Chemistry, Academia Sinica, Taipei, 11529 Taiwan, ROC*
[c]*Department of Chemistry, National Taiwan University, Taipei, 10617 Taiwan, ROC*

Received 27 March 2007; accepted 27 March 2007

The CeO_2–Co_3O_4 binary oxide was prepared by impregnation of the high surface area Co_3O_4 support (S.A. = 100m^2 g^{-1}) with cerium nitrate (20 wt% cerium loading on Co_3O_4). Pretreatment of CeO_2–Co_3O_4 binary oxide was divided both methods: reduction (under 200 and 400 °C, assigned as CeO_2–Co_3O_4–R200 and CeO_2–Co_3O_4–R400 and calcination (under 350 and 550 °C, assigned as CeO_2–Co_3O_4–C350 and CeO_2–Co_3O_4–C550). The binary oxides were investigated by means of X-ray diffraction (XRD), nitrogen adsorption at −196 °C, infrared (IR), transmission electron microscopy (TEM), diffuse reflectance spectroscopy (DRS) and temperature programmed reduction (TPR). The results showed that the binary oxides pretreatment under low-temperatures possessed larger surface area. The cobalt phase of binary oxides also was transferred upon the treating temperature, i.e., the CeO_2–Co_3O_4–R200 binary oxide exhibited higher surface area (S.A. = 109m^2 g^{-1}) and the main phase was CeO_2,Co_3O_4 and CoO. While, the CeO_2–Co_3O_4–R400 binary oxide exhibited lower surface area (S.A. = 40m^2 g^{-1}) and the main phase was CeO_2, CoO and Co. Apparently, the optimized pretreatment of CeO_2–Co_3O_4 binary oxide can control both the phases and surface area.

KEY WORDS: CeO_2–Co_3O_4 binary oxide; phase transformation; X-ray diffraction.

1. Introduction

Transition metal oxides are becoming more important in several fields of materials technology, i.e., carbon dioxide lasers [1], catalytic combustion [2], mine rescue devices [3] and the CO sensor [4]. This importance promotes studies purpose for better understanding of the surface reactivity of metal oxides.

Low temperature abatement of carbon monoxide is important in environmental pollution control [5]. There are several reports describing the use of noble metals for CO oxidation at ambient temperatures [6–10]. In order to lower the price, considerable attention has been paid to various transition metal oxides and mixed metal oxides. Among these metal oxides, cobaltic oxide (Co_3O_4) is very attractive for the presence of mobile oxygen in Co_3O_4 [9–11]. The high activity of Co_3O_4 on CO oxidation is likely to be due to the relatively low ΔH of vaporization of O_2 [12,13]. This means that the Co–O bond strength of Co_3O_4 is relatively weak, leading to provide easily reactive oxygen from the lattice oxygen. In our studies, we also observe that the activity of Co_3O_4 toward CO oxidation is enhanced significantly by increasing the surface area (S.A.) [10]. This means that increasing the S.A. of Co_3O_4 mainly due to a weakening in the strength of the Co–O bond and the acceleration of oxygen desorption from Co_3O_4. Thus, many researchers have measured the catalytic activity of Co_3O_4 for CO oxidation [11,14].

Ceria (CeO_2) has a high oxygen storage capacity and well known catalytic and red-ox properties (couples of Ce^{4+}/Ce^{3+}), making more oxygen available for the oxidation process [15]. The rapid growth in the applications and the characterization of CeO_2-containing catalysts has been documented [16–23]. In particular, the CuO/CeO_2 catalyst was reported to be very active for the complete CO oxidation and even comparable to noble metals [17]. Good catalytic activity is also observed for high surface area CoO_x/CeO_2 composite catalysts [20].

In the previous study, we have proved that the activity of CeO_2–Co_3O_4 binary oxide for CO oxidation is depended on the pretreatments [24]. The most active sample is pretreatment under 200 °C reduction. Further, the studied object of this work is aimed to understand the correlations between the effect of pretreatment conditions on the CeO_2–Co_3O_4 binary oxide and phase transformation of cobalt oxide. The characteristics of materials are employed by means of X-ray diffraction (XRD), nitrogen adsorption at −196 °C, transmission electron microscopy (TEM), infrared (IR), diffuse reflectance spectroscopy (DRS) and temperature-programmed reduction (TPR).

*To whom correspondence should be addressed.
E-mail: chiensh@gate.sinica.edu.tw

2. Experimental

2.1. Preparation of CeO-Co_3O_4 binary oxide

The high-valence cobalt oxide was synthesized first with precipitation-oxidation method in an aqueous solution, then, refined by a controlled hydrogen reduction in a temperature-programmed reduction system till 230 °C to get cobaltic oxide. The detailed preparation procedure was described in a previous paper [8].

The CeO_2–Co_3O_4 binary oxide was prepared by impregnation of the Co_3O_4 support with an aqueous solution of the desired concentration of $Ce(NO_3)_3\,6H_2O$ (Aldrich, the ceria loading is 20 wt%). The sample was dried at 110 °C for 24 h, followed by both pretreatment methods: reduction in a H_2 stream for 2 h (under 200 and 400 °C, assigned as CeO_2–Co_3O_4–R200 and CeO_2–Co_3O_4–R400) and calcination in an air stream (under 350 and 550 °C, assigned as CeO_2–Co_3O_4–C350 and CeO_2–Co_3O_4–C550) for 4 h.

2.2. Characterization techniques

X-ray diffraction (XRD) measurements were performed using Siemens D5000 diffractometer with Cu $K_{\alpha 1}$ radiation ($\lambda = 1.5405$ Å) at 40 kV and 30 mA with a scanning speed in 2θ of 2 ° min^{-1}. Diffraction peaks of crystalline phase were compared with those of standard compounds reported in the JCPDS 2002 data file (Co_3O_4: 73-1701; CoO: 71-2391; Co: 88-4307; CeO_2: 81-0792). The crystallite sizes of cobaltic oxide and ceria were estimated using the Scherrer equation.

Nitrogen adsorption isotherms at −196 °C were determined volumetrically with Micrometritics ASAP 2010. The catalysts were pre-outgassed at 5×10^{-5} Torr for 3 h at 110 °C. The surface area was determined from the nitrogen adsorption isotherm.

CeO_2–Co_3O_4 binary oxides were characterized using TEM (Hitachi H600-3). The samples for the electron microscopy were prepared by making an ethanol suspension and deposited onto an undercoat of a holey carbon film.

The infrared spectra were obtained by a Bomen DA-8 spectrometer in the range of 500–800 cm^{-1}. One milligram of each powder sample was diluted with 200 mg of vacuum-dried IR-grade KBr and subjected to a pressure of 8 tons.

The DRS spectra were measured at room temperature on a Hitachi U3410 spectrophotometer equipped with an integration sphere. The spectra were recorded against a $BaSO_4$ standard in the region 200–800 nm.

Reduction behavior of CeO_2–Co_3O_4 binary oxides were studied by temperature-programmed reduction (TPR). About 25 mg of the sample was heated in a flow of 10% H_2/He gas mixture at a flow rate of 10 ml min^{-1}. During TPR, the temperature was programmed to rise with 10 °C min^{-1} to 550 °C.

3. Results and discussion

The XRD patterns of both ceria and cobaltic oxide are shown in figure 1. Based on the diffraction peaks, we can distinguish the phase components of CeO_2–Co_3O_4 binary oxide. Figure 2 shows the XRD patterns of CeO_2–Co_3O_4–C350 and CeO_2–Co_3O_4–C550. The XRD patterns of CeO_2–Co_3O_4–R200 and CeO_2–Co_3O_4–R400 are appeared in figure 3. All samples of XRD profiles show a well-crystallized CeO_2 phase with a fluorite-type structure. Besides the CeO_2 phase, a separate crystalline Co_3O_4 [figures 2(a) and (b) and 3(a)], CoO [figure 3(a) and (b)] and Co [figure 3(b)] species are found in the CeO_2–Co_3O_4 binary oxides. The degree of crystalline of both phases (Co_3O_4 and CeO_2) increases with increasing calcined temperature [figure 2(a) and (b)], while the crystallite size is similar under 350 and 550 °C calcined (~8 nm for Co_3O_4 and ~6.0 nm for CeO_2). Also, the degree of crystalline of mixed phases and CeO_2 increases with increasing reduced temperature [figure 3(a) and (b)]. The crystallite size of CeO_2 is not affected under low or high reduced temperature (~6.0 nm), while the effect of treating temperature under reduced atmosphere is apparent for both component and crystallite size. According to the diffraction patterns and the width of the (200) diffraction pattern of CoO crystalline, the component of CeO_2–Co_3O_4–R200 [figure 3(a)] is a mixed phases [Co_3O_4 and CoO, although the (311) peak of Co_3O_4 overlap with the (111) peak of CoO, the faint peak of (311) diffraction pattern can be further characterized by TPR] and the crystallite size of CoO is 8.3 nm. As the reducing temperature increases, the component of CeO_2–Co_3O_4–R400 shows CoO and Co mixed phases and the crystallite size of CoO grows to 9.4 nm. The components of CeO_2–Co_3O_4 binary oxides under different treatments are summarized in the 4th column of table 1. Slight change of particle size for cobaltic oxide explains that the introducing of ceria can help in improving the dispersion of Co_3O_4.

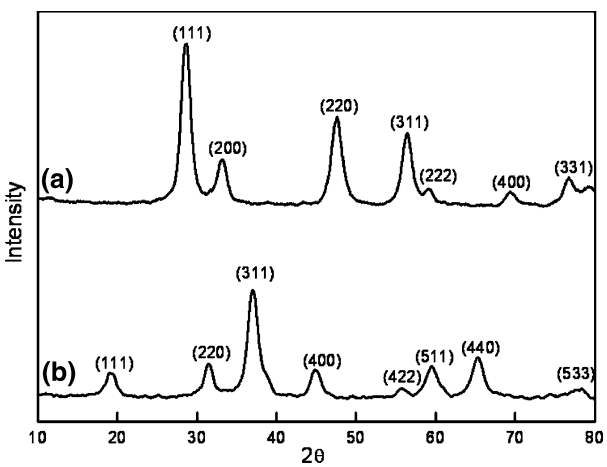

Figure 1. The XRD characterization of ceria and cobaltic oxide: (a) CeO_2; (b) Co_3O_4.

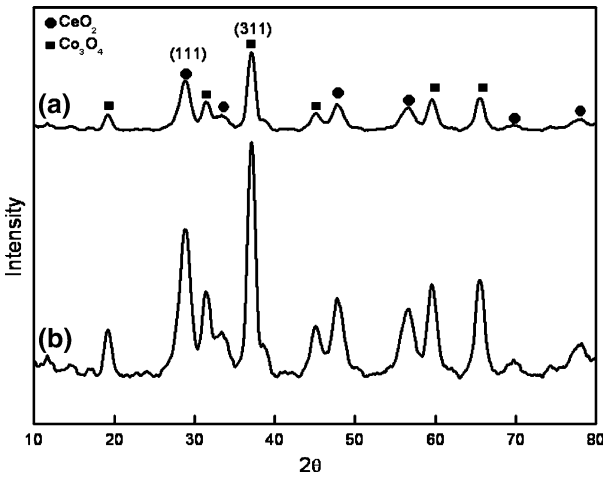

Figure 2. The XRD characterization of CeO_2–Co_3O_4 binary oxides: (a) CeO_2–Co_3O_4–C350; (b) CeO_2–Co_3O_4–C550.

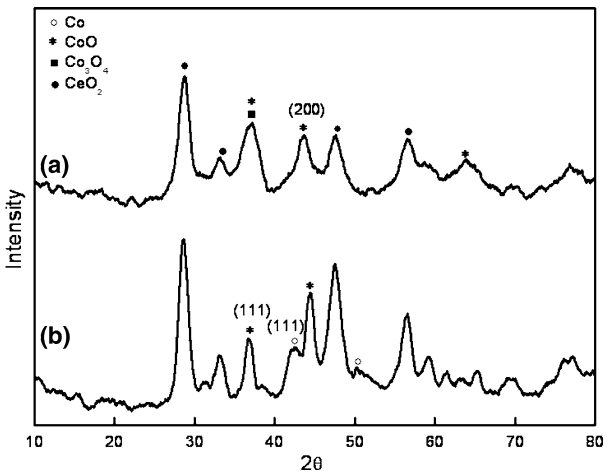

Figure 3. The XRD characterization of CeO_2–Co_3O_4 binary oxides: (a) CeO_2–Co_3O_4–R200; (b) CeO_2–Co_3O_4–R400.

Figure 4 presents the N_2 adsorption–desorption isotherm plots of ceria, cobaltic oxide and the CeO_2–Co_3O_4 binary oxides at 77 K. Obtained surface areas of CeO_2–Co_3O_4 binary oxides are summarized in the 9th

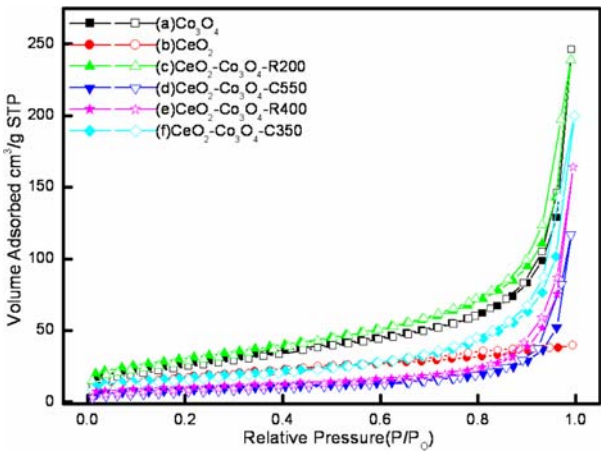

Figure 4. N_2 adsorption-desorption isotherm plots of ceria, cobaltic oxide and the CeO_2–Co_3O_4 binary oxides.

column of table 1. The results show that the optimized pretreatment can obtain high surface area of CeO_2–Co_3O_4 binary oxide. The increase in treating temperature induces a decrease in its surface area [i.e., CeO_2–Co_3O_4–C550 (S.A. = 31m^2 g^{-1}) < CeO_2–Co_3O_4–C350 (S.A. = 60m^2 g^{-1}); CeO_2–Co_3O_4–R400 (S.A. = 40m^2 g^{-1}) < CeO_2–Co_3O_4–R200 (S.A. = 109m^2 g^{-1})]. The induced decrease due to the thermal treatment might be attributed to grain growth of the particles or collapse of pores [25]. The smaller nanoparticles of the binary oxide are consistent with the higher surface areas. From the increasing of crystalline and decreasing of surface area of mixed oxides under high temperatures treating condition, a possible explanation was the sintering of nanoparticles. The aggregation of nanoparticles can be observed with the TEM image. Figure 5 shows the TEM images of CeO_2–Co_3O_4–R200 [figure 5(a)] and CeO_2–Co_3O_4–R400 [figure 5(b)] samples. Apparently, the dispersion of CeO_2–Co_3O_4–R200 is better than the CeO_2–Co_3O_4–R400 (mean particle sizes increase from about 7 to 20 nm). The significant aggregation under high temperature reduction induces the decrease of surface area of binary oxide. In order to gain further insight into the microstructural characteristics of the

Table 1
Characterization of CeO_2–Co_30_4 binary oxides

Sample	Pretreatments (°C)		Components[a]	Cystalline sizes (nm)[b]				S.A. (m^2 g^{-1})	TPR (°C)		
	Reduction	Calcination		CeO_2	Co_3O_4	CoO	Co		CeO_2 surface	Co_3O_4	
										α	β
Co_3O_4			Co_3O_4	–	8.2	–	–	100	–	281	390
CeO_2			CeO_2	6.0	–	–	–	64	503	–	–
CeO_2–Co_3O_4–C350		350	CeO_2,Co_3O_4	6.0	9.8	–	–	60	–	312	375
CeO_2–Co_3O_4–C550		550	CeO_2,Co_3O_4	6.0	9.8	–	–	31	–	333	380
CeO_2–Co_3O_4–R200	200		CeO_2,Co_3O_4, CoO	6.0	8.0	8.3	–	109	–	260	360
CeO_2–Co_3O_4–R400	400		CeO_2, CoO, Co	6.0	–	9.4	6.2	40	–	–	290

[a] Phases from XRD data by JCPDS pattern; [b]Calculated the Scherrer equation according to the diffraction peaks.

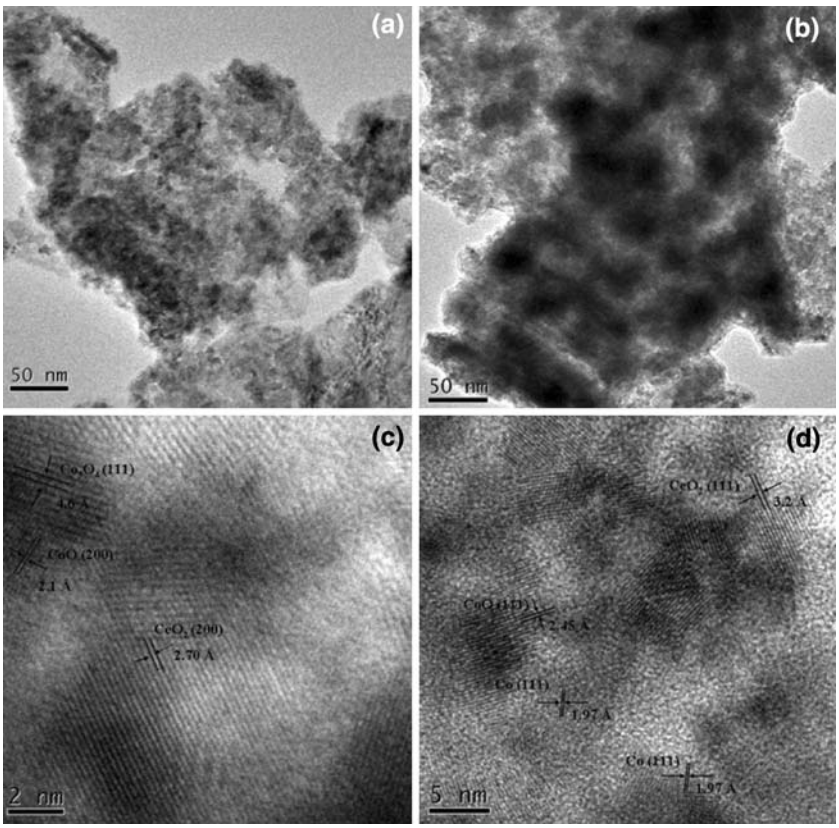

Figure 5. Microscopy images of CeO_2–Co_3O_4 binary oxides: (a) TEM image of CeO_2–Co_3O_4–R200; (b) TEM image of CeO_2–Co_3O_4–R400; (c) HRTEM image of CeO_2–Co_3O_4–R200; (d) HRTEM image of CeO_2–Co_3O_4–R400.

binary oxides, HRTEM analyses are performed and show in figure 5(c) [CeO_2–Co_3O_4–R200] and (d) [CeO_2–Co_3O_4–R400]. Different lattice fringe patterns are observed for both samples. The labeled species in figure 5(c) corresponds to Co_3O_4 [lattice fringe at 4.6 Å for (111) plane], CoO [lattice fringe at 2.1 Å for (200) plane] and CeO_2 [lattice fringe at 2.70 Å for (200) plane]. Whereas the labeled species in figure 5(d) shows other components: CoO [lattice fringe at 2.45 Å for (111) plane], Co [lattice fringe at 1.97 Å for (111) plane] and CeO_2 [lattice fringe at 3.2 Å for (111) plane]. These results are in good agreement with those obtained from XRD analysis.

Figure 6 shows the IR transmittance spectra of ceria, cobaltic oxide and the CeO_2–Co_3O_4 binary oxides. All samples except CeO_2 and CeO_2–Co_3O_4–R400 [figure 5(a) and (f)] show two distinct bands at 575–578 (v_1) and 660–663 (v_2) cm^{-1} that originated by the stretching vibrations of the Co–O bond of cobaltic oxide [24,26,27]. The v_1 band is characteristic of $OB^{os}{}_3$ (where B^{os} denotes the Co^{3+} in octahedral hole) vibration and the v_2 band is attributed to the $A^{ts}B^{os}O_3$ (where A^{ts} denotes the Co^{2+} in tetrahedral hole) vibration in the spinel lattice [24,28,29]. At the same time, the two bands shift apparently to a lower wavenumber for CeO_2–Co_3O_4–R200 [figure 6(e)] due to the surface of smaller nanoparticle (higher surface area) crystals to weaken the Co–O bond strength. The redistribution of free electrons between the surface and the bulk cause a decrease of the bond force constant, and consequently absorption red shifts.

The DRS spectral features are sensitive to nano-sized oxide particles [30]. The existence of Co_3O_4 is further confirmed by the DRS spectroscopy. The DRS spectra of ceria, cobaltic oxide and the CeO_2–Co_3O_4 binary oxides are shown in figure 7. Both maxima characteristic bands at 720 and 420 nm [see figure 7(b)–(e)] are due to the existence of Co_3O_4 [24,31,32] where a migration to octahedral sites occurs. Herein it is worth noting that these bands become more intense as the surface area of catalyst increased. Pure CeO_2 [figure 7(a)] shows a broad absorption feature with an absorption edge around 400 nm characteristic of the semiconducting nature [33,34]. The maximum characteristic band for pure CeO_2 or CeO_2–Co_3O_4 binary oxides at 305 nm [see figure 7(a) and (c)–(f)] corresponds to the localized O $\rightarrow$ Ce charge transfer transition involving a number of surface Ce^{4+} ions. Therefore the DRS results are in good agreement with XRD and IR analysis.

In order to understand the Co–O bond strength of CeO_2–Co_3O_4 binary oxides, further diagnosed with TPR technique to understand the reduction behavior of CeO_2–Co_3O_4 binary oxides. Figure 8 shows the TPR profiles for ceria, cobaltic oxide and the CeO_2–Co_3O_4

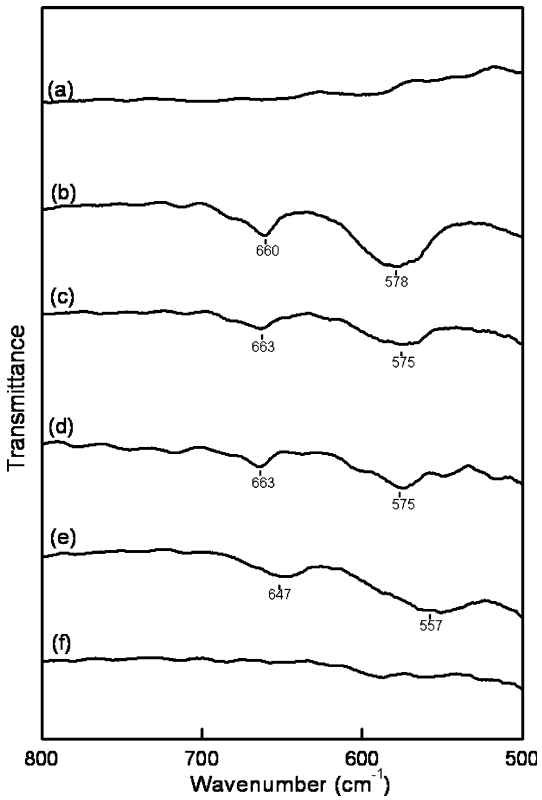

Figure 6. The IR characterization of ceria, cobaltic oxide and the CeO_2–Co_3O_4 binary oxides: (a) CeO_2; (b) Co_3O_4; (c) CeO_2–Co_3O_4–C350; (d) CeO_2–Co_3O_4–C550; (e) CeO_2–Co_3O_4–R200; (f) CeO_2–Co_3O_4–R400.

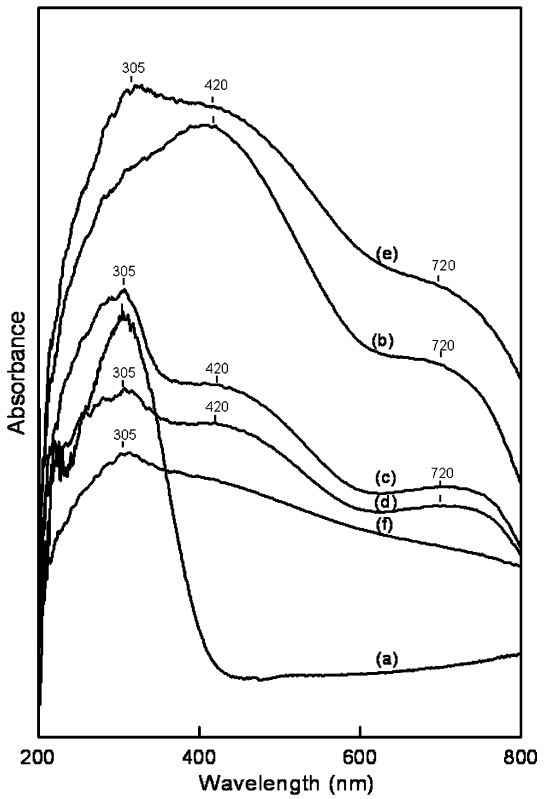

Figure 7. The DRS spectra of ceria, cobaltic oxide and the CeO_2–Co_3O_4 binary oxides: (a) CeO_2; (b) Co_3O_4; (c) CeO_2–Co_3O_4–C350; (d) CeO_2–Co_3O_4–C550; (e) CeO_2–Co_3O_4–R200; (f) CeO_2–Co_3O_4–R400.

binary oxides. All the samples except CeO_2 and CeO_2–Co_3O_4–R400 [figure 8(a) and (f)] exhibit a similar TPR profile, consisting of two well-resolved reduction peaks (assigned as α peak and β peak). These profiles point to a two-step reduction process: the first one (α peak) of low intensity, starts at low temperature and overlaps with the more intense second one (β peak). According to the literature [8,10,20,35,36] , with the subsequent structural change to CoO, which followed the higher-temperature β peak and is due to the reduction of CoO to metallic cobalt [equation (2)].

$$Co_3O_4 + H_2 \rightarrow 3CoO + H_2O \quad (1)$$

$$CoO + H_2 \rightarrow Co + H_2O \quad (2)$$

As can be seen in figure 8(b)–(e) and the last two columns of table 1, apparently shift of the α peak and β peak appears under different treatments which are relationship with the surface area of binary oxides. Compared to the S.A. (the 9th column of table 1), both the α peak and β peak shift to lower temperatures as the surface area increases, i.e., the α peak and β peak of CeO_2–Co_3O_4–R200 binary oxide (S.A. = $109 m^2 g^{-1}$) is 260 and 360 °C [figure 8(e)], respectively. While, the α peak and β peak of CeO_2–Co_3O_4–C550 binary oxide (S.A. = $31 m^2 g^{-1}$) is 333 and 380 °C [figure 8(d)], respectively. These results indicate that the increasing of surface area of CeO_2–Co_3O_4 binary oxides can weaken the bond strength of Co–O and promote more lattice oxygen desorbed from Co_3O_4 to decrease the reduction temperature. Aside from the consecutive reduction of Co_3O_4, a reduction peak with lower intensity at 503 °C [figure 8(a)] is presented for pure CeO_2. The peak is attributed to the removal of surface capping oxygen ions during the reduction reaction [37,38]. Moreover, the reduction behavior of β peak in CeO_2–Co_3O_4 binary oxides [figure 8(c)–(e)] and pure Co_3O_4 [figure 8(b)] are some different. The tailing β peak in CeO_2–Co_3O_4 binary oxides is attributed to the reduction of capping oxygen of ceria. From the shift of reduction temperatures, the combined effect between the CeO_2 and Co_3O_4 is more evident for the low temperature reduction treated CeO_2–Co_3O_4–R200 binary oxides. Also, it is interesting to compare the reduction behavior of CeO_2–Co_3O_4–R400 and CeO_2–Co_3O_4–R200 binary oxides. This is in agreement with the results of XRD analysis. Different mixed phases obtained under reducing conditions give various diffraction patterns and reduction behavior. A consecutive reduction for Co_3O_4 species [exist in CeO_2–Co_3O_4–R200 sample, see figures 3(a) and 8(e)] and a single peak for CoO at 290 °C [exist in CeO_2–Co_3O_4–R400 binary oxides, see figures 3(b) and 8(f)] are observed separately. Since via 400 °C reducing condition has removed the

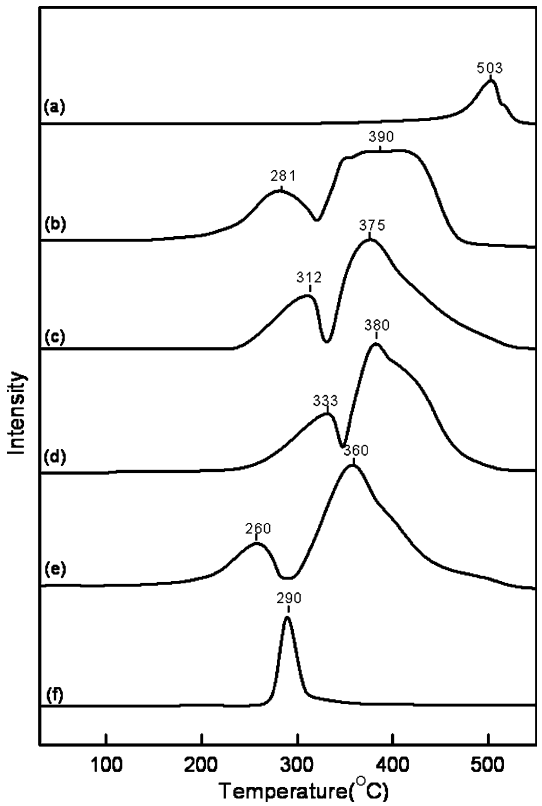

Figure 8. The TPR profiles of ceria, cobaltic oxide and the CeO_2–Co_3O_4 binary oxides: (a) CeO_2; (b) Co_3O_4; (c) CeO_2–Co_3O_4–C350; (d) CeO_2–Co_3O_4–C550; (e) CeO_2–Co_3O_4–R200; (f) CeO_2–Co_3O_4–R400.

capping oxygen of ceria, no tailing peak occurs in CeO_2–Co_3O_4–R400 binary oxides.

4. Conclusion

A series of CeO_2–Co_3O_4 binary oxides have been obtained by different pretreatment conditions and characterized. The following conclusions are displayed:

(1) Phase components of CeO_2–Co_3O_4 binary oxides and surface area can be controlled under optimized pretreatment.
(2) The CeO_2–Co_3O_4 binary oxides possess larger surface area under low-temperatures pretreatment, i.e., CeO_2–Co_3O_4–R200 (S.A. = $109 m^2 g^{-1}$) > CeO_2–Co_3O_4–R400 (S.A. = $40 m^2 g^{-1}$).
(3) Phase components of CeO_2–Co_3O_4 binary oxides are transferred upon the treating temperature, i.e., the CeO_2–Co_3O_4–R200 binary oxide exhibits CeO_2, Co_3O_4 and CoO, while, the CeO_2–Co_3O_4–R400 binary oxide exhibits CeO_2, CoO and Co.

Acknowledgments

We are pleased to acknowledge financial supports for this study from Academia Sinica and the National Science Council of the Republic of China.

References

[1] S.D. Gardner, G.B. Hoflund, D.R. Schryer, J. Schryer, B.T. Upchurch and E.J. Kielin, Langumir 7 (1991) 2135.
[2] D.L. Trimm, Appl. Catal. A 7 (1983) 249.
[3] A.B. Lamb, C. Bray and J.C.W. Fraser, Ind. Eng. Chem. 12 (1920) 213.
[4] H. Yamaura, K. Moriya, N. Miura and N. Yamazoe, Sens. Actuators B 65 (2000) 39.
[5] D.R. Schryer, B.T. Upchurch, B.D. Sidney, K.G. Bromn, G.B. Hoflund and P.K. Herz, J. Catal. 130 (1991) 314.
[6] Y. Kim, S.K. Shi and J.H. White, J. Catal. 61 (1980) 61.
[7] M. Olsbye, R. Wendelbo and T. Akporiayc, Appl. Catal. A 152 (1997) 127.
[8] H.K. Lin, C.B. Wang, H.C. Chiu and S.H. Chien, Catal. Lett. 86 (2003) 63.
[9] H.K. Lin, H.C. Chiu, H.C. Tsai, S.H. Chien and C.B. Wang, Catal. Lett. 88 (2003) 169.
[10] C.B. Wang, C.W. Tang, S.J. Gau and S.H. Chien, Catal. Lett. 101 (2005) 59.
[11] P. Broqvist, I. Panas and H. Person, J. Catal. 210 (2002) 198.
[12] M. Haneda, Y. Kintaichi, N. Bion and H. Hamada, Appl. Catal. B 46 (2003) 473.
[13] B.A. Sazonov, V.V. Popovskii and G.K. Boreskov, Kinet. Catal. 9 (1968) 255.
[14] D.S. Lafyatis, G.P. Ansell, S.C. Bennett, J.C. Frost, P.J. Millington, R.R. Rajaram, A.P. Walker and T.H. Ballinger, Appl. Catal. B 18 (1998) 123.
[15] A. Martinez-Arias, M. Fernandez-Garcia, O. Galvez, J.M. Coronado, J.A. Anderson, J.C. Conesa, J. Soria and G. Munuera, J. Catal. 195 (2000) 207.
[16] M.A. Centeno, C. Portales, I. Carrizosa and J.A. Odriozola, Catal. Lett. 102 (2005) 289.
[17] W. Liu and F.S. Maria, J. Catal. 153 (1995) 304.
[18] U. Oran and D. Uner, Appl. Catal. B 54 (2004) 183.
[19] M.F. Luo, Y.J. Zhong, X.X. Yuan and X.M. Zheng, Appl. Catal. A 162 (1997) 121.
[20] M. Kang, M.W. Song and C.H. Lee, Appl. Catal. A 251 (2003) 143.
[21] A. Trovarelli, Catal. Rev. 38 (1996) 439.
[22] A. Martinez-Arias, M. Fernandez-Garcia, J. Soria and J.C. Conesa, J. Catal. 182 (1999) 367.
[23] M.M. Natile and A. Glisenti, Chem. Mater. 15 (2003) 2502.
[24] C.W. Tang, C.C. Kuo, M.C. Kuo, C.B. Wang and S.H. Chien, Appl. Catal. A 309 (2006) 37.
[25] G.A. El-Shobaky and N.M. Deraz, Mater. Lett. 47 (2001) 231.
[26] C. Spenser and D. Schroeder, Phys. Rev. B 9 (1974) 3658.
[27] T. Andrushkevich, G. Boreskov, V. Popovskii, L. Pliasova, L. Karakchiev and A. Ostankovitch, Kinet. Katal. 6 (1968) 1244.
[28] St.G. Christoskova, M. Stoyanova, M. Georgieva and D. Mehandjiev, Mater. Chem. Phys. 60 (1999) 39.
[29] R.N. Singh, J.P. Pandey, N.K. Singh, B. Lal, P. Chartier and J.F. Koenig, Electrochim. Acta 45 (2000) 1911.
[30] B.M. Weckhuysen and R.A. Schoonheydt, Catal. Today 49 (1999) 441.
[31] M. Lojacono, A. Cimino and G.C.A. Schuit, Gazz. Chim. Ital. 103 (1973) 1281.
[32] F.J. Gillambias, A.L. Agudo and V. Rives-Arnau, J. Mater. Sci. 17 (1982) 936.
[33] S.P. Tandon and J.P. Gupta, Phys. Stat. Sol. 38 (1970) 363.
[34] A. Bensalem, F.B. Verduraz, M. Delamar and G. Bugli, Appl. Catal. A 121 (1995) 81.
[35] P. Arnoldy and J.A. Moulijn, J. Catal. 93 (1985) 38.
[36] M. Voβ, D. Borgmann and G. Wedler, J. Catal. 212 (2002) 10.
[37] G.R. Rao, H.R. Sahu and B.G. Mishra, Colloids surf. A 220 (2003) 261.
[38] X.C. Zheng, S.P. Wang, X.Y. Wang, S.R. Wang, X.G. Wang and S.H. Wu, Mater. Lett. 59 (2005) 2769.